Opto-Electronic Advances

Supplementary information

2022, Vol. 5, No. 3

DOI: 10.29026/oea.2022.210026

Ultrafast multi-target control of tightly focused light fields

Yanxiang Zhang[1†], Xiaofei Liu[2†], Han Lin[3], Dan Wang[1], Ensi Cao[1], Shaoding Liu[1], Zhongquan Nie[1*] and Baohua Jia[3*]

[1]Key Lab of Advanced Transducers and Intelligent Control System, Ministry of Education and Shanxi Province, College of Physics and Optoelectronics, Taiyuan University of Technology, Taiyuan 030024, China; [2]Department of Physics, Harbin Institute of Technology, Harbin 150001, China; [3]Centre of Translational Atomaterials (CTAM), Faculty of Science, Engineering and Technology, Swinburne University of Technology, Hawthorn, VIC 3122, Australia.

[†]These authors contributed equally to this work.

[*]Correspondence: ZQ Nie, E-mail: niezhongquan@tyut.edu.cn; BH Jia, E-mail: bjia@swin.edu.au

This file includes:

Supplementary information for this paper is available at https://doi.org/10.29026/oea.2022.210026

Section 1: Linearly-polarized light illumination

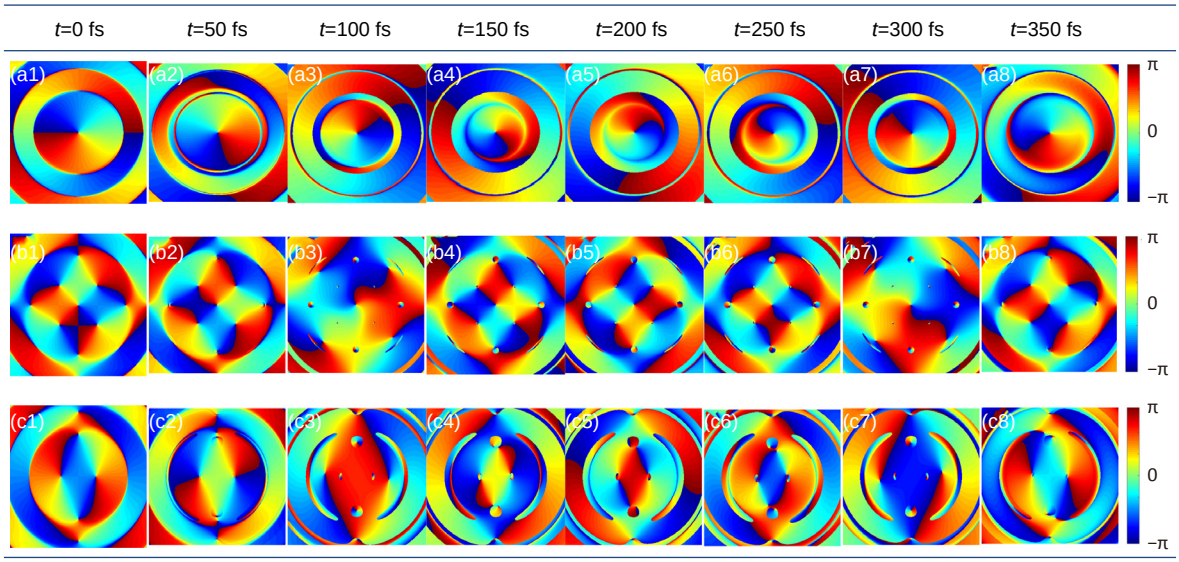

Fig. S1 | A phase gallery of tightly focused linearly polarized light with first-order vortex at different temporal intervals. The phase distributions of the transverse $|\boldsymbol{E}_x|^2$ (**a1**–**a8**), $|\boldsymbol{E}_y|^2$ (**b1**–**b8**) and longitudinal $|\boldsymbol{E}_z|^2$ (**c1**–**c8**) in the x–y plane with the time of t = 0 fs (a1–c1), 50 fs (a2–c2), 100 fs (a3–c3), 150 fs (a4–c4), 200 fs (a5–c5), 250 fs (a6–c6), 300 fs (a7–c7), and 350 fs (a8–c8), respectively. The sizes for all of the images are 2λ×2λ. Parameters are the same as those in Fig. 2.

For a linearly polarized light excitation, the varying process (Movie SL3) of the y-component fields is that the four side lobes first disappear, and then the main lobes begin to disappear as well. When t = 107 fs, the main lobes reappear in the central region. With the change of time, both the main lobes and the side lobes gradually become bright, reaching the brightest fields near t = 200 fs. After t = 250 fs, the darkening process is that the main lobes disappear initially accompanied with a clockwise rotation, and subsequently the side lobes gradually vanish. On the contrary, the bright process is that the side lobes approximate to the positions of the main lobes and then replace the main lobes entirely. In a similar fashion, the side lobes start to brighten with an ultrafast rotation during this time interval. Finally, the overall y-component fields transfer to the initial state again around t = 400 fs. It should be emphasized that the ultrafast manipulation of x-component and z-component fields has been elucidated in the main text.

As for the longitudinal field component of linearly polarized light illumination (see Fig. 2), we discover that the eye-popping rotational phenomena appear, which evokes our extremely intense research interests in ultrafast optical tweezers and spanners. In this respect, few researchers have revealed half-period rotated characteristics of time-assisted focal light fields with different polarization-vortex orders[1,2]. Despite such intriguing properties, the rotation of light field is based on the rotation of the incoming field rather than over ultrashort time, as reported in present manuscript. We notice from Fig. S2(a) and S2(b) that when the time t < 0, the focal fields rotate anticlockwise while they turn into clockwise rotation if t > 0. That is, the sign of wave-front phase related to that of time is responsible for the resultant rotation orientation of optical fields[3]. The straight rotation process of the z component field (i.e., dynamic processes and the angle representations) is animatedly displayed in Movie SL4 and in Fig. S2. The rotation procedure is showcased as follows: t = 100 fs (see Fig. S2(b)), the optical field intensity exhibits a tiny value and the rotation angle equals to 15° relative to 0 fs; t =102 fs (see Fig. S2(c)), the principal lobe divides into half from the center and its intensity declines clearly. Meanwhile, the field rotation proceeds to occur and its revolving angle is twice as large as Fig. S2(b); t =120 fs (see Fig. S2(d)), the more side lobes appear in off-focus region and the main lobe holds lower intensity, as well as the focal optical field rotated 90° exactly with respect to 0 fs; t = 200 fs (see Fig. S2(e)), the main lobe gradually brighten and simultaneously rotate a significant angle of 105°; t =300 fs (see Fig. S2(f)), two inner side lobes come together to form a new main lobe. Moreover, the main lobe rotates an angle of 165° compared with the initial time. In fact, the total focal field pattern is able to rebound to the original state (t = 0 fs) when the time increase to around 400 fs.

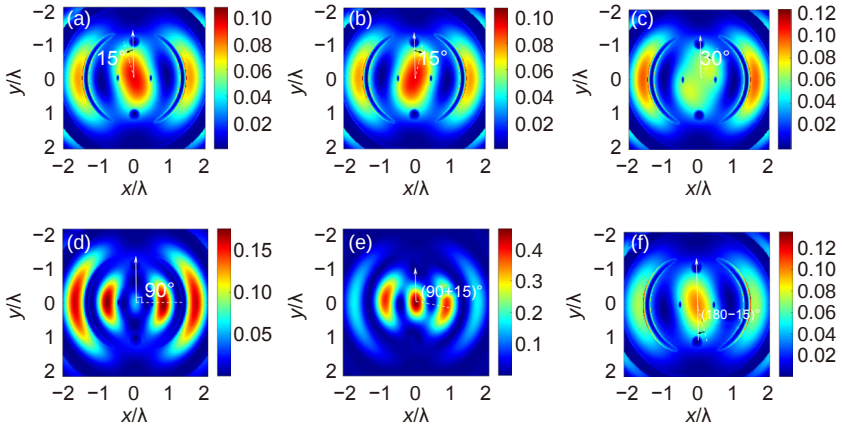

Fig. S2 | Longitudinal field component of tightly focused vectorial vortex beams with rotational angle representation of linearly polarized light in the *x*−*y* plane with (a) *t* = -100 fs, (b) *t* = 100 fs, (c) *t* = 102 fs, (d) *t* = 120 fs, (e) *t* = 200 fs, (f) *t* = 300 fs, respectively.

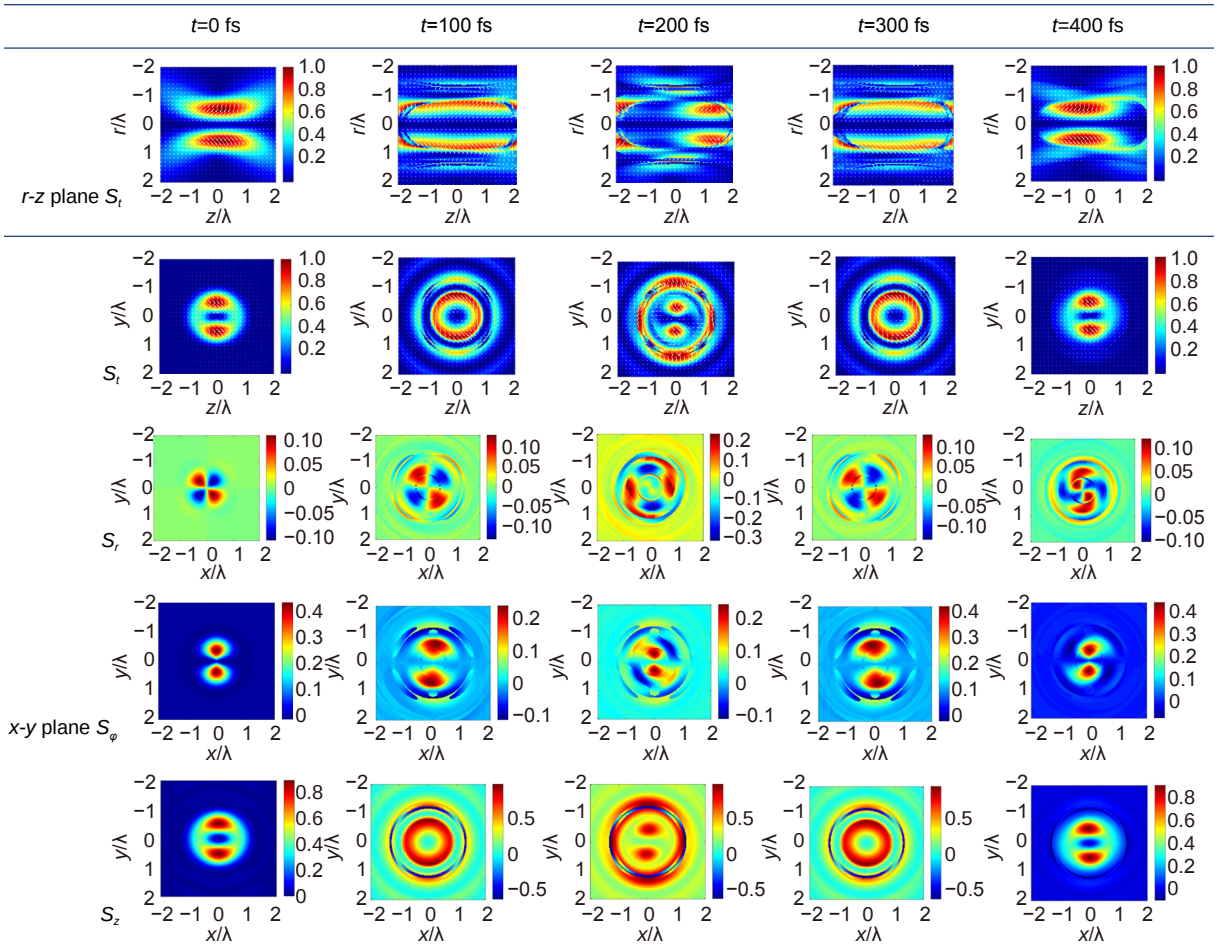

Fig. S3 | Normalized Poynting vector fields and the energy flows (white arrows) along the propagating direction (the first row) and on the focal plane (the second to last rows) of the tightly focused linearly polarized beams when *t* = 0 fs, 100 fs, 200 fs, 300 fs, 400 fs. The total Poynting vector fields and the energy flows (the first row and the second row); radial Poynting vector fields S_r (the third row) and azimuthal Poynting vector fields S_φ (the fourth row) as well as longitudinal Poynting vector fields S_z (the last row).

Section 2: Comparing linearly and radially polarized illumination

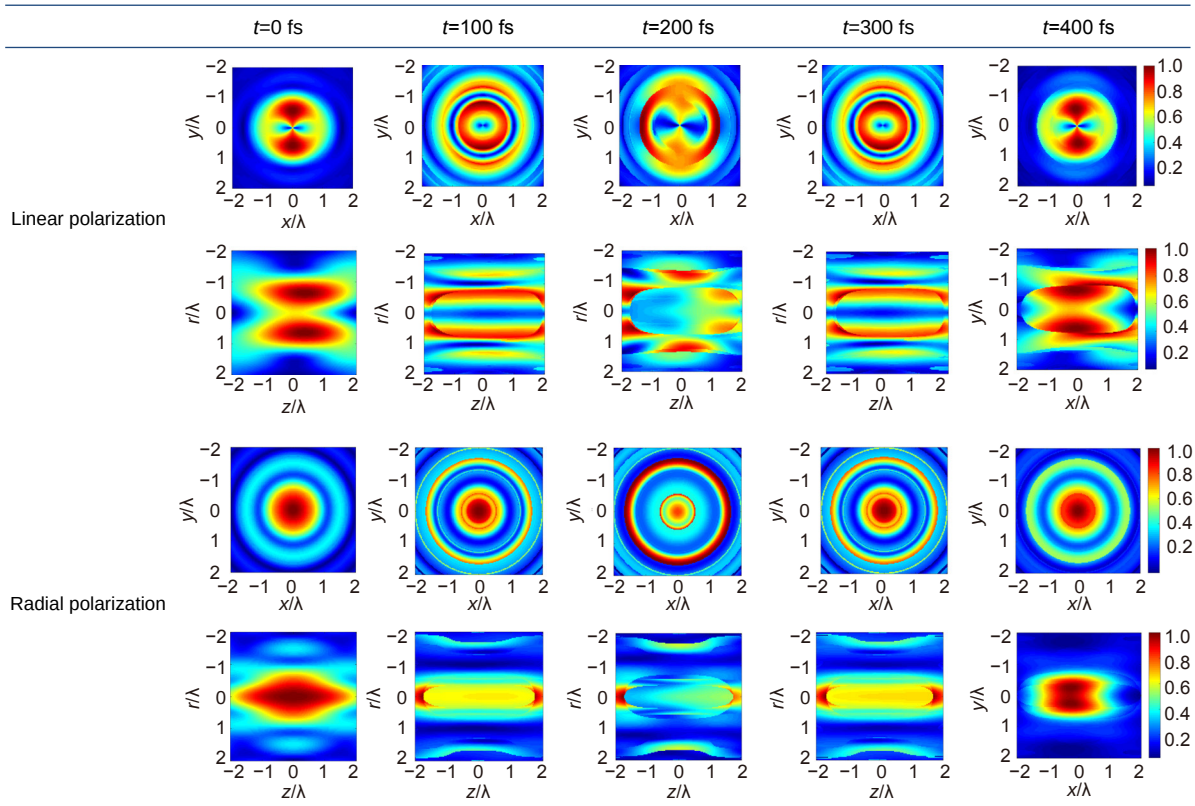

Fig. S4 | Magnetic field distributions of linearly polarized illumination (first and second rows) and radially polarized illumination (third and fourth rows) in the *x*−*y* plane (first and third rows) and *r*−*z* plane (second and forth rows) with *t* = 0 fs, *t* = 100 fs, *t* = 200 fs, *t* = 300 fs, *t* = 400 fs, respectively.

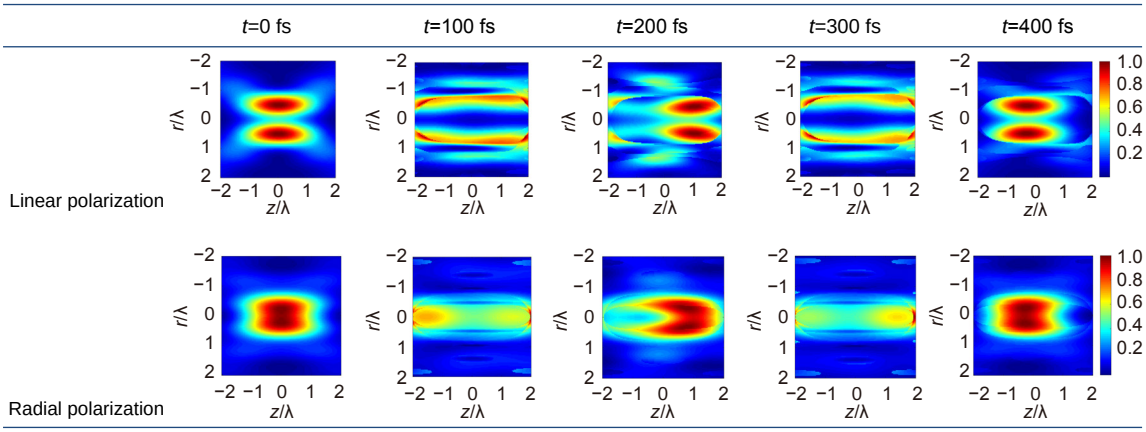

Fig. S5 | The total focal field distributions of linearly polarized light illumination (first row) and the radially polarized light illumination (second row) in the *r*−*z* plane with *t* = 0 fs, *t* = 100 fs, *t* = 200 fs, *t* = 300 fs, *t* = 400 fs, respectively.

Section 3: Azimuthally-polarized light illumination

According to the Richards-Wolf vectorial diffraction theory[4–6], the electric field distribution in the focal region of an azimuthally polarized vortex-dressed Laguerre–Gaussian femtosecond pulse light focused by a high NA objective lens can be expressed as,

$$\boldsymbol{E}(r,\varphi,z,\omega) = \frac{-\mathrm{i}kf}{2\pi}\int_0^{\alpha}\int_0^{2\pi} \boldsymbol{S}(\theta,\omega)\exp(\mathrm{i}m\phi)\sin\theta\sqrt{\cos\theta}\exp\left[\mathrm{i}kr\sin\theta\cos(\phi-\varphi)+\mathrm{i}kz\cos\theta\right]\boldsymbol{P}_3(\theta,\phi)\,d\phi d\theta\,, \tag{S1}$$

where the unit polarized matrix[7,8],

$$\boldsymbol{P}(\theta,\phi) = -\sin\phi\boldsymbol{i} + \cos\phi\boldsymbol{j} + 0\boldsymbol{k}\ . \tag{S2}$$

The local field in the time domain $\boldsymbol{E}(r, \varphi, z, t)$ can be described by separately Fourier transforming each vector component of $\boldsymbol{E}(r, \varphi, z, \omega)$. Equation (S1) can be rewritten as:

$$\boldsymbol{E}_x(r,\varphi,z,t) = \frac{f}{2c}\int_0^{\infty}\int_0^{\alpha}\omega\boldsymbol{S}(\theta,\omega)\sin\theta\sqrt{\cos\theta}\exp\left[\omega\left(\frac{z}{c}\cos\theta - t\right)\right](I_{m+1} - I_{m-1})\,\mathrm{d}\theta\mathrm{d}\omega\ ,$$

$$\boldsymbol{E}_y(r,\varphi,z,t) = -\frac{\mathrm{i}f}{2c}\int_0^{\infty}\int_0^{\alpha}\omega\boldsymbol{S}(\theta,\omega)\sin\theta\sqrt{\cos\theta}\exp\left[\mathrm{i}\omega\left(\frac{z}{c}\cos\theta - t\right)\right](I_{m+1} + I_{m-1})\,\mathrm{d}\theta\mathrm{d}\omega\ ,$$

$$\boldsymbol{E}_z(r,\varphi,z,t) = 0. \tag{S3}$$

From the Maxwell's equations, the relationship between the electric field and magnetic field is determined by:

$$\boldsymbol{H} = -\frac{\mathrm{i}}{k}\mathrm{rot}\boldsymbol{E}, \tag{S4}$$

where

$$\mathrm{rot}\boldsymbol{E} = (\partial_y\boldsymbol{E}_z - \partial_z\boldsymbol{E}_y)\,\boldsymbol{i} - (\partial_x\boldsymbol{E}_z - \partial_z\boldsymbol{E}_x)\,\boldsymbol{j} + (\partial_x\boldsymbol{E}_y - \partial_y\boldsymbol{E}_x)\,\boldsymbol{k}. \tag{S5}$$

Hence, three-independent magnetic field components in the focal plane can be derived in the following form:

$$[\boldsymbol{H}_x, \boldsymbol{H}_y, \boldsymbol{H}_z] = -\frac{\mathrm{i}}{k}\left[\partial_y\boldsymbol{E}_z - \partial_z\boldsymbol{E}_y, \partial_z\boldsymbol{E}_x - \partial_x\boldsymbol{E}_z, \partial_x\boldsymbol{E}_y - \partial_y\boldsymbol{E}_x\right]. \tag{S6}$$

The partial differential in Eq. (11) can be resolved by considering the recursive relation of the Bessel function: $\mathrm{J}_m'(x) = \mathrm{J}_{m-1}(x) - \frac{m}{x}\mathrm{J}_m(x)$.

For azimuthally polarized light illumination (see Fig. S6), it is clearly seen that the total focal field (see Fig. 3(a1)–(a8)) and its two transverse field components (see Fig. 3(b1)–(b8) and Fig. 3(c1)–(c8)) implement rich distributions while the longitudinal field component (see Fig. 3(d1)) equal to zero with the passage of time. As for the total fields firstly, the initial central bright spot with single ring begins to shift into multi-ring structures and then go back to the state of t = 0 fs. Secondly, the iso-intensity transverse field components show the rotational distributions which possess the same variation of radially polarized light illumination as time elapsed. It is noticed that for the azimuthally polarized light illumination there is only the rotational feature in the focal plane but no the light-dark alternation and transverse/longitudinal polarization conversion owing to the lacked z-component field.

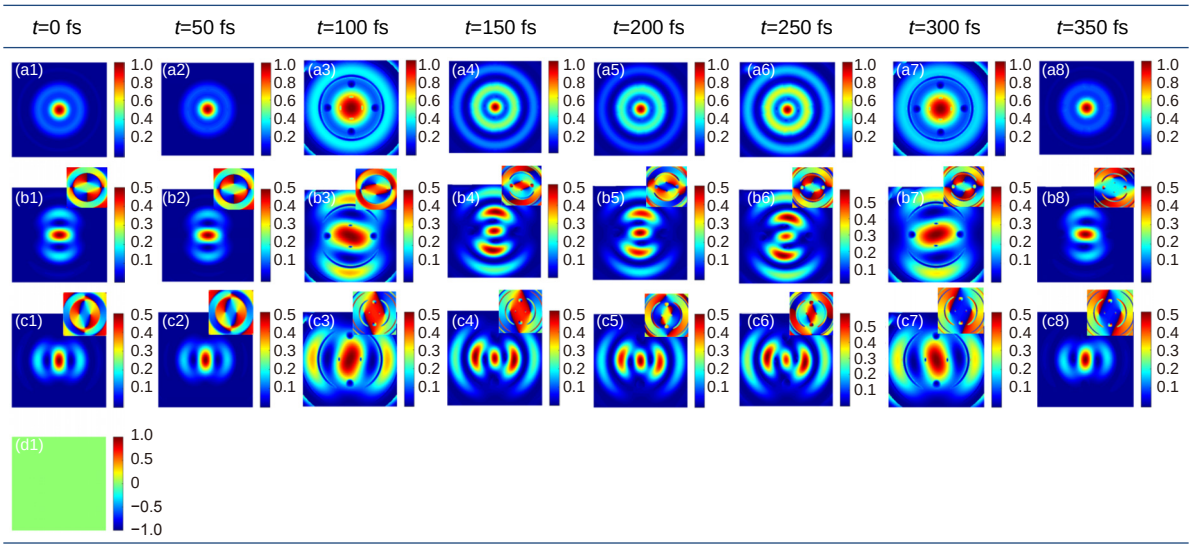

Fig. S6 | The focal light field distributions of azimuthally polarized light illumination with first-order vortex at different temporal intervals. The total intensity distributions $|\boldsymbol{E}_t|^2$ (**a1**–**a8**) as well as the transverse $|\boldsymbol{E}_x|^2$ (**b1**–**b8**), $|\boldsymbol{E}_y|^2$ (**c1**–**c8**) and the longitudinal $|\boldsymbol{E}_z|^2$ = 0 (**d1**) field distributions in the x–y plane when t = 0 fs (a1–d1), 50 fs (a2–c2), 100 fs (a3–c3), 150 fs (a4–c4), 200 fs (a5–c5), 250 fs (a6–c6), 300 fs (a7–c7), and 350 fs (a8–c8), respectively. The phase distributions inset in the corresponding light field distributions in Figs. (b1)–(b8) and (c1)–(c8). Parameters are the same as those in Fig. 2.

Section 4: Conceptually experimental paradigm

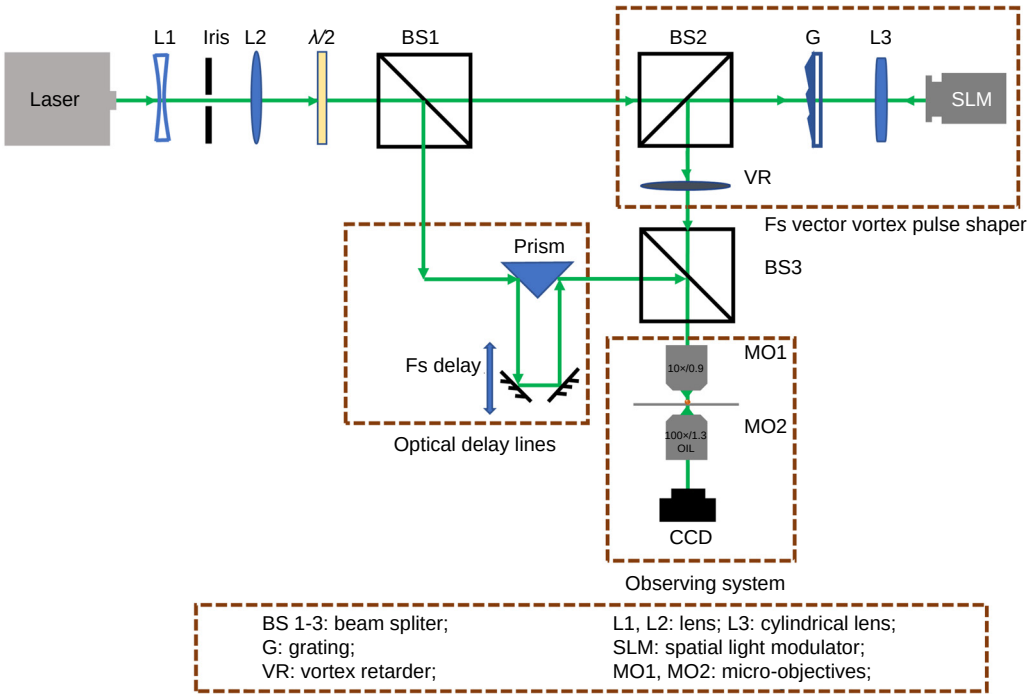

Fig. S7 | Schematic of the optical setup for synthesizing the controllable ultrafast multi-target light fields using three detachable systems. Bottom inset: Definitions of the symbols used to identify the optical components in the setup.

We now have successfully generated various cylindrical (radially and azimuthally polarized) vector beams and detect their tightly focused light fields. For example, we have experimentally synthesized high-quality radially and azimuthally polarized beams utilizing the femtosecond laser pulse, as shown in Fig. S8. Also, the tightly focused (NA=0.9) light fields of these ultrafast radially and azimuthally polarized (vortex) beams were visualized in Fig. S9. These preliminary advances are observed at a static time (t = 0 fs).

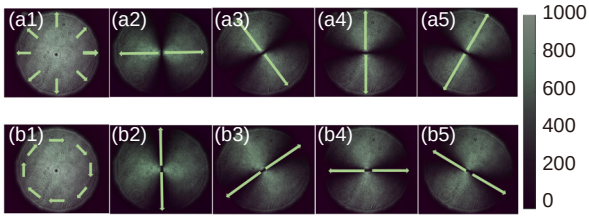

Fig. S8 | Experimentally synthetic radially and azimuthally polarized beams. (**a1**)–(**a5**) the radially polarized beams; (**b1**)–(**b5**) the azimuthally polarized beams. The green arrows denote distinct transmitted directions of the polarization analyzer.

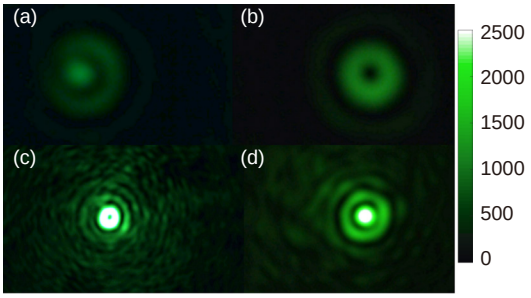

Fig. S9 | The tightly focused light fields at 0 fs of (**a**) radially polarized beam; (**b**) azimuthally polarized beams; (**c**) radially polarized beam with 1-order vortex phase; (**d**) azimuthally polarized beams with 1-order vortex phase.

Section 5: Statements of the direction of Poynting vector

As shown in Fig. S10(a) and 10(b), the horizontal and vertical arrows denote pure transverse and longitudinal energy flux, respectively. In Fig. S10(c), we defined a tilt angle ψ to quantize the proportion amount between two orthogonal energy fluxes according to $\psi = \tan^{-1}(\sqrt{S_r^2 + S_\phi^2}/S_z^2)$. That is, the transverse energy flow is prevailing when $\psi < 45°$; hence the corresponding longitudinal electric field plays a major role, and vice versa. Therefore, it is convenient to judge the conversion of polarized component fields through the redistributed energy flux.

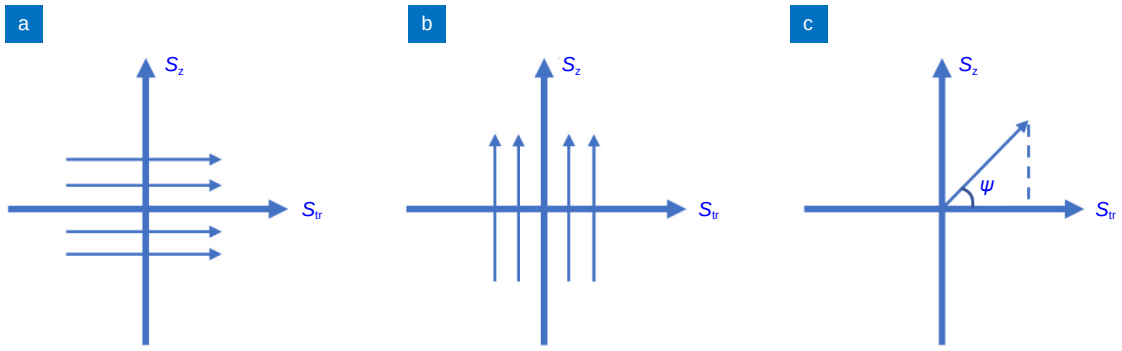

Fig. S10 | The direction of Poynting vector for interpreting the polarization conversion between two orthogonal component fields.

Section 6: The case if the objective lens has aberration

As a matter of fact, we implement the control of ultrafast multi-target light fields via an aplanatic high numerical aperture objective lens. According to previous researches, for an ideal imaging system the remaining parts of aberration, such as coma, distortion, astigmatism etc., almost have no influence on the outcomes and thus they can be ignored. However, it is impossible to eliminate aberration of objective lens for the practical scenarios. In order to illustrate this statement, we present the optical field distributions under distinct aberration following refs. 9 and 10,

$$\boldsymbol{E}(r,\varphi,z,\omega) = -\frac{\mathrm{i}kf}{2\pi}\iint \boldsymbol{S}(\theta,\omega)\exp(\mathrm{i}m\phi)\sin\theta \boldsymbol{A}(\theta,\phi)\boldsymbol{P}(\theta,\phi)\exp[\mathrm{i}kr\sin\theta\cos(\phi-\varphi)+\mathrm{i}kz\cos\theta]\mathrm{d}\theta\mathrm{d}\phi\ , \tag{S7}$$

here, $\boldsymbol{E}(r, \varphi, z, \omega)$ is the electric field vector at the point of (r, φ, z) expressed in a cylindrical coordinate whose origin locates at the ideal focal point of the objective lens, $\boldsymbol{P}(\theta, \phi)$ is matrix unit vector about the polarization of the incident beam, $\boldsymbol{A}(\theta, \phi)$ denotes the wavefront aberration function of the objective lens and usually three primary aberrations in the beam can be expressed as:

Spherical aberration: $\boldsymbol{A}(\theta,\boldsymbol{\phi}) = \exp\left[\mathrm{i}k\boldsymbol{A}_\mathrm{s}\left(\frac{\sin\theta}{\sin\boldsymbol{\alpha}}\right)^4\right]$,

coma: $\boldsymbol{A}(\theta,\phi) = \exp\left[\mathrm{i}k\boldsymbol{A}_\mathrm{c}\left(\frac{\sin\theta}{\sin\alpha}\right)^3\cos\phi\right]$,

astigmatism: $\boldsymbol{A}(\theta,\phi) = \exp\left[\mathrm{i}k\boldsymbol{A}_\mathrm{a}\left(\frac{\sin\theta}{\sin\alpha}\right)^2\cos^2\phi\right]$,

where $\boldsymbol{A}_\mathrm{s}$, $\boldsymbol{A}_\mathrm{c}$, $\boldsymbol{A}_\mathrm{a}$ denote aberration coefficients. For an ideal imaging system, we can assume that $\boldsymbol{A}_\mathrm{s}$, $\boldsymbol{A}_\mathrm{c}$, $\boldsymbol{A}_\mathrm{a}$ are all equal to zero. By a Fourier-transformation, the electric fields of the femtosecond pulse in the vicinity of the focal spot can be calculated by the superposition of each spectral component as,

$$\boldsymbol{E}_i(r,\varphi,z,t) = \int \boldsymbol{E}_i(r,\varphi,z,\omega)\exp(-\mathrm{i}\omega t)\,\mathrm{d}\omega, i = x,y,z. \tag{S8}$$

Section 7: The pulse-width-dependent ultrafast multi-target light fields

To further clarify the dependence of ultrafast multi-target light fields on the pulse width, we have performed the tightly focused light field distributions of radially polarized beam with distinct pulse width of 8 fs and 10 fs at different time intervals, respectively, as shown in Figs. S11 and S12. It is found from Figs. S11 and S12 that the spatial rotation and polarization conversion between two orthogonal field components still exist, while the bright-dark alternative feature in the total fields is not so obvious. Therefore, we suspect that the multi-target fields might be sensitive to shorter laser pulse.

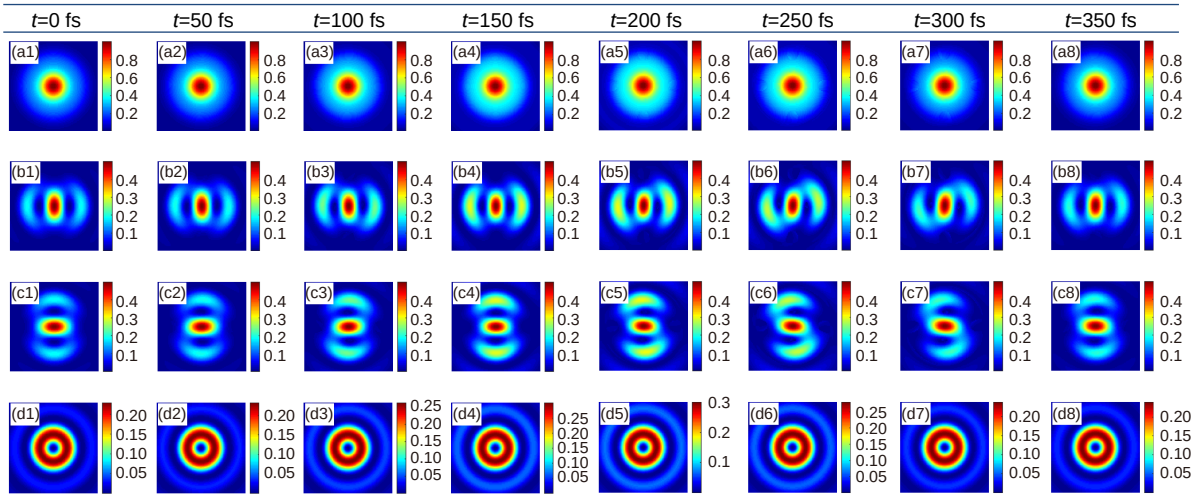

Fig. S11 | The tightly focused field distributions of radially polarized light with the 1-order vortex phase at different temporal intervals and with pulse width of 8 fs.

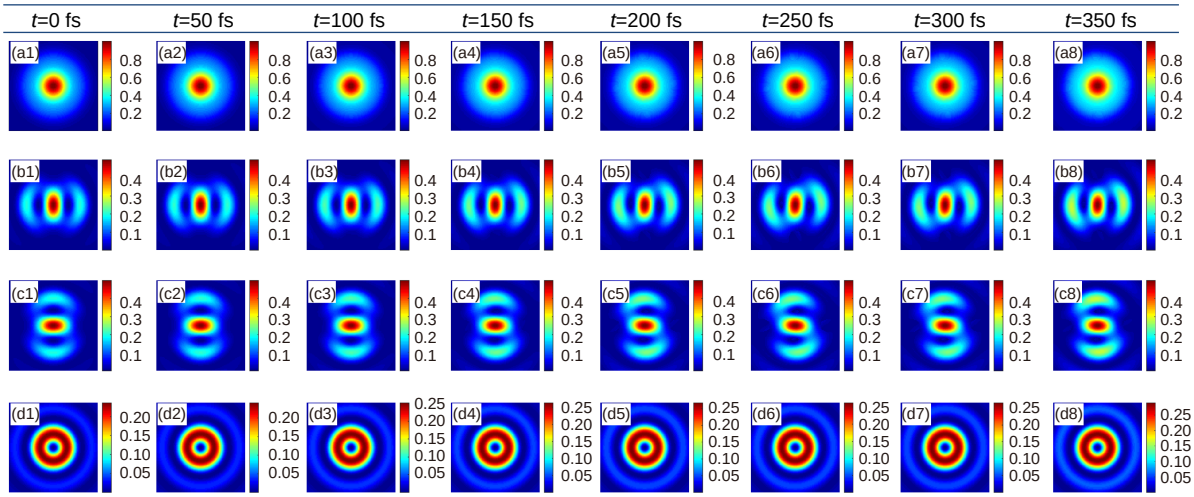

Fig. S12 | The tightly focused field distributions of radially polarized light with the 1-order vortex phase at different temporal intervals and with pulse width of 10 fs.

Section 8: The tightly focused light fields in between 400fs – 1 ps

It can be observed from Fig. S13 that the overall field and its three field components at 400 fs possess consistent distributions of that at 0 fs [see Fig. S13(a1)–(d1)]. As time elapses from 400 fs to 1 ps, we find from Fig. S13(a1)–(a8) that the total fields display obvious extensions at the time of odd multiples of 100 fs (i.e., 500 fs, 700 fs and 900 fs), while basically maintain invariability at the time of even times of 100 fs (i.e., 400 fs, 600 fs, 800 fs and 1000 fs). Furthermore, the *x*-field components show the similar patterns with the total fields due to the dominant roles in total fields [see Fig. S13(b1)–(b8)]. The difference between them is that the spatial rotations exist in *x*- components, whereas there is no such feature in overall fields. Analogous to that from 0 fs to 400 fs, we don't consider the *y*- components because of the tiny magnitudes, which is order of magnitude smaller [see Fig. S13(c1)–(c8)]. It is shown from Fig. S13(d1)–(d8) that with time variation, there remains the polarization conversions between *x*- and *z*- components.

Unlike that from 0 fs to 400 fs for radially polarized light illumination, the bright-dark alternation in the total fields as time elapses from 400 fs to 1 ps vanishes as shown in Fig S14(a1)–(a8). Interestingly, the spatial rotation features are still retaining as time goes [see Fig. S14(b1)–(b8) and Fig. S14(c1)–(c8)]. Moreover, the reciprocal conversions between two orthogonal polarized field components also unfold in Fig. S14(d1)–(d8).

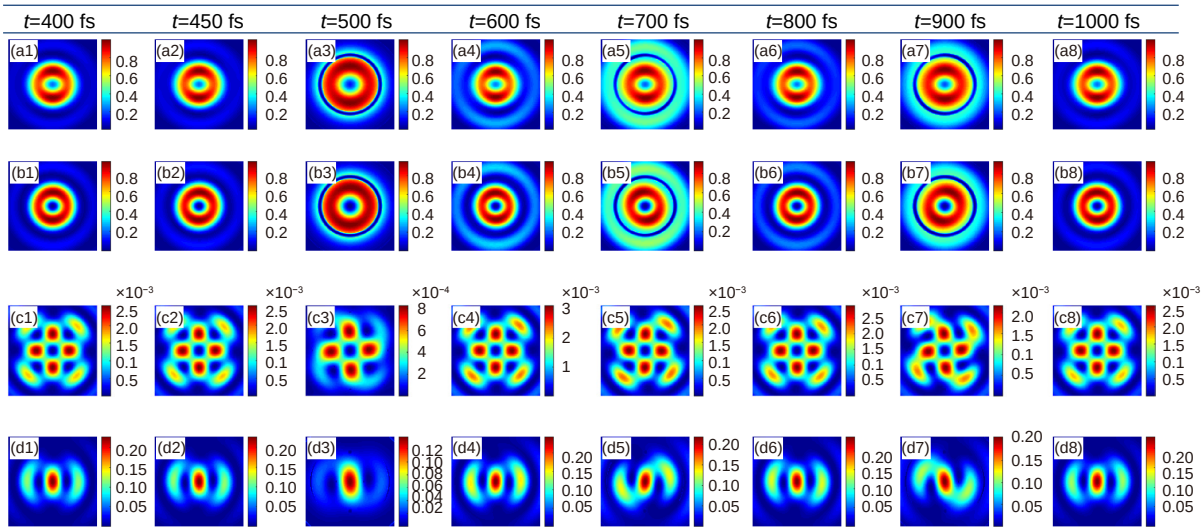

Fig. S13 | The tightly focused field distributions of linearly polarized light with the first-order vortex phase at different temporal delays in between 400 fs – 1 ps.

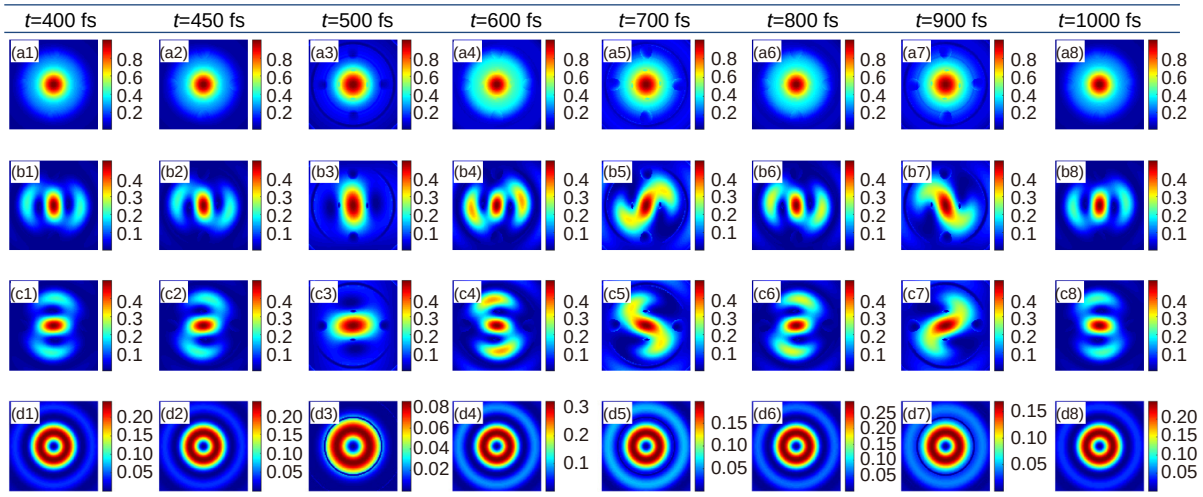

Fig. S14 | The focused field distributions of radially polarized light with the first-order vortex phase at different temporal delays in between 400 fs – 1 ps.

Section 9: The tightly focused radially polarized light fields with m = 2, 3

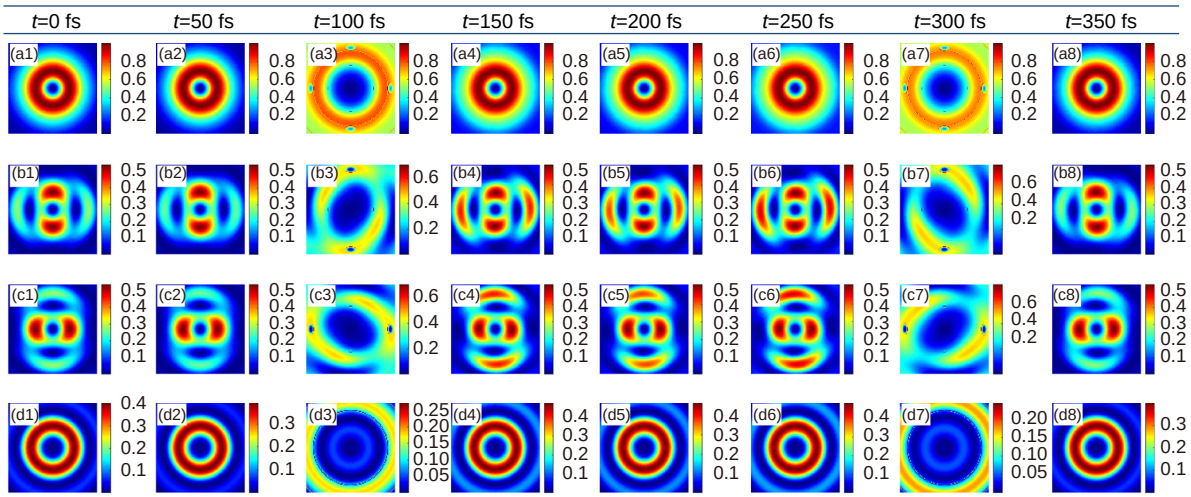

Fig. S15 | The tightly focused field distributions of radially polarized light with the 2-order vortex phase at different temporal intervals from 0 fs – 350 fs.

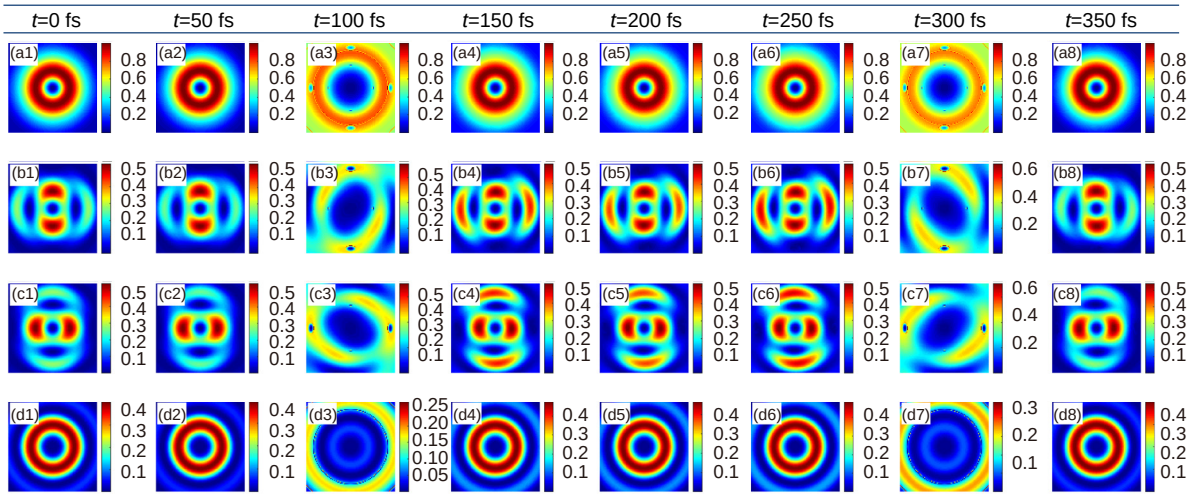

Fig. S16 | The tightly focused field distributions of radially polarized light with the 3-order vortex phase at different temporal intervals from 0 fs – 350 fs.

Supplemental movies

The vividly detailed visual representations of linearly polarized, radially polarized, azimuthally polarized (longitudinal field components equal to zero) total field, x field component, y field component and z field component are exhibited from Movie SL1 to SA3, respectively.

Movie SL1. The total field intensity distribution focusing of *linearly polarized light* with first-order vortex at different times.

Movie SL2. The x-component field intensity distribution focusing of *linearly polarized light* with first-order vortex at different times.

Movie SL3. The y-component field intensity distribution focusing of *linearly polarized light* with first-order vortex at different times.

Movie SL4. The z-component field intensity distribution focusing of *linearly polarized light* with first-order vortex at different times.

Movie SR1. The total field distributions focusing of *radially polarized light* with first-order vortex at different times.

Movie SR2. The x-component field distributions focusing of *radially polarized light* with first-order vortex at differ-

ent times.

Movie SR3. The *y*-component field distributions focusing of *radially polarized light* with first-order vortex at different times.

Movie SR4. The *z*-component field distributions focusing of *radially polarized light* with first-order vortex at different times.

Movie SA1. The total field distributions focusing of *azimuthally polarized light* with first-order vortex at different times.

Movie SA2. The *x*-component field distributions focusing of *azimuthally polarized light* with first-order vortex at different times.

Movie SA3. The *y*-component field distributions focusing of *azimuthally polarized light* with first-order vortex at different times.

References

1. Khonina SN, Golub I. Time behavior of focused vector beams. *J Opt Soc Am A* **33**, 1948–1954 (2016).
2. Khonina SN, Golub I. Ultrafast rotating dipole or propeller-shaped patterns: subwavelength shaping of a beam of light on a femtosecond time scale. *Opt Lett* **41**, 1605–1607 (2016).
3. Chong A, Wan CH, Chen J, Zhan QW. Generation of spatiotemporal optical vortices with controllable transverse orbital angular momentum. *Nat Photonics* **14**, 350–354 (2020).
4. Wolf E. Electromagnetic diffraction in optical systems-I. An integral representation of the image field. *Proc Roy Soc London A Math Phys Sci* **253**, 349–357 (1959).
5. Richards B, Wolf E. Electromagnetic diffraction in optical systems, II. Structure of the image field in an aplanatic system. *Proc Roy Soc London A Math Phys Sci* **253**, 358–379 (1959).
6. Lin H, Jia BH, Gu M. Generation of an axially super-resolved quasi-spherical focal spot using an amplitude-modulated radially polarized beam. *Opt Lett* **36**, 2471–2473 (2011).
7. Tian B, Pu JX. Tight focusing of a double-ring-shaped, azimuthally polarized beam. *Opt Lett* **36**, 2014–2016 (2011).
8. Pu JX, Zhang ZM. Tight focusing of spirally polarized vortex beams. *Opt Laser Technol* **42**, 186–191 (2010).
9. Kant R. An analytical method of vector diffraction for focusing optical systems with Seidel aberrations II: astigmatism and coma. *J Mod Opt* **42**, 299–320 (1995).
10. Deng SH, Liu L, Cheng Y, Li RX, Xu ZZ. Effects of primary aberrations on the fluorescence depletion patterns of STED microscopy. *Opt Express* **18**, 1657–1666 (2010).